



## Computational adaptive optics for polarization-sensitive optical coherence tomography

JIANFENG WANG,<sup>1</sup> ERIC J. CHANEY,<sup>1</sup> EDITA AKSAMITIENE,<sup>1</sup> MARINA MARJANOVIC,<sup>1,2,3</sup> AND STEPHEN A. BOPPART<sup>1,2,3,4,\*</sup>

<sup>1</sup>Beckman Institute for Advanced Science and Technology, University of Illinois at Urbana-Champaign, 405 N. Mathews Ave., Urbana, Illinois 61801, USA

<sup>2</sup>Department of Bioengineering, University of Illinois at Urbana-Champaign, Urbana, Illinois 61801, USA

<sup>3</sup>Carle Illinois College of Medicine, University of Illinois at Urbana-Champaign, Urbana, Illinois 61801, USA

<sup>4</sup>Department of Electrical and Computer Engineering, University of Illinois at Urbana-Champaign, Urbana, Illinois 61801, USA

\*Corresponding author: boppart@illinois.edu

Received 6 January 2021; revised 20 February 2021; accepted 10 March 2021; posted 23 March 2021 (Doc. ID 418637); published 21 April 2021

**Defocus aberration in optical systems, including optical coherence tomography (OCT) systems employing Gaussian illumination, gives rise to the well-known compromise between transverse resolution and depth-of-field. This results in blurry images when out-of-focus, whilst other low-order aberrations (e.g., astigmatism, coma, etc.) present in both the OCT system and biological samples further reduce image resolution and contrast. Computational adaptive optics (CAO) is a computed optical interferometric imaging technique that modifies the phase of the OCT data in the spatial frequency domain to correct optical aberrations and provide improvement of the image quality throughout the three-dimensional (3D) volume. In this Letter, we report the first implementation of CAO for polarization-sensitive OCT to correct defocus and other low-order aberrations, providing enhanced polarization-sensitive imaging contrast (i.e., intensity and phase retardation) on a 3D OCT phantom, molded plastics, *ex vivo* chicken breast tissue, and *ex vivo* human breast cancer tissue.** © 2021 Optical Society of America

<https://doi.org/10.1364/OL.418637>

Optical coherence tomography (OCT) is an established imaging technique based on the principle of low coherence interferometry [1]. Combining micrometer-scale optical resolution, high-speed, and millimeter-scale imaging depth, OCT has found wide clinical applications in ophthalmology [2], oncology [3], and gastroenterology [4], among others. OCT, as with other three-dimensional (3D) optical imaging modalities, suffers from limited depth-of-field, resulting from its inherent defocus aberration and blurring regions of OCT images that are out-of-focus. In addition, the OCT imaging beam is often distorted due to imperfect optics and/or refractive index variations in the imaged sample, further degrading the OCT image quality throughout its imaging volume. In recent years, computational optical imaging techniques have been proposed, developed,

and demonstrated to mitigate the adverse effects of optical aberrations on OCT image quality. In particular, our group has successfully demonstrated interferometric synthetic aperture microscopy (ISAM) and computational adaptive optics (CAO) [5–7]. ISAM is a solution to the coherent microscopy inverse problem, corrects defocus for all depths, and provides spatially invariant transverse resolution through an efficient Fourier domain coordinate transformation [5]. On the other hand, CAO modifies the phase of the OCT data in the spatial frequency domain to correct optical aberrations (e.g., defocus, astigmatism, coma, etc.) without using a deformable mirror, as is commonly done in hardware-based adaptive optics [6,7].

Polarization-sensitive OCT (PS-OCT) is a functional extension of OCT that measures the polarization state changes of the backscattered light from the imaged sample (e.g., breast [8], skin [9], muscle [10], polymers [11], etc.) [12]. Birefringent samples are characterized by a refractive index that depends on the input polarization orientation and on the propagation direction of light inside the sample, making it possible to use PS-OCT to probe the sample birefringence. Jones calculus can be used to model the PS-OCT system, where the sample birefringence introduces phase retardation (PR) between the two components of the Jones vector that can be measured using a PS-OCT system [12]. As in OCT, defocus and other optical aberrations degrade PS-OCT imaging contrast. Our group has previously demonstrated PS-ISAM [13] to correct the defocus aberration for PS-OCT, while the other low-order optical aberrations were left uncorrected. In this Letter, we report the first implementation of CAO to correct both defocus and other low-order aberrations of PS-OCT imaging and validate its contrast improvement performance on different samples. Using a low-numerical-aperture (NA) (i.e., 0.1) scan objective, the longitudinal polarization of PS-OCT is greatly overwhelmed by the power in the transverse polarization, supporting the use of the Jones vector representation at low-NA as in the standard

PS-OCT model [13] and allowing the application of computational optical imaging techniques including CAO [6,7] on each component of the measured Jones vector, followed by standard PS processing to derive intensity and PR [14]. The intensity image sharpness, calculated as the summation of intensity raised to a power of two, was chosen to optimize the Zernike weight selected for CAO implementation [7,15]. The Sobel image metric was used to characterize the PS (i.e., PR, optical axis, etc.) parameter sharpness [13,16]. Experimental data for this Letter were acquired with a spectral domain PS-OCT system that has been reported elsewhere [14]. The axial and transverse resolutions of the system were 5  $\mu\text{m}$  and 8  $\mu\text{m}$ , respectively. Further, a quarter waveplate (AHWP05M-1600, Thorlabs) was placed at the sample arm of the PS-OCT system, and the PR was measured at  $\sim 1.47$ , which is close to the theoretical value of 1.57, quantitatively confirming the PR accuracy derived from the system. In addition, since the reliability of the PR values depend on the OCT intensity signal-to-noise ratio (SNR), only when we could identify image features from the OCT intensity images did we trust the corresponding PR map regions.

To demonstrate CAO correction for PS-OCT, a commercially available OCT phantom (APL-OP01, Arden Photonics, UK) was imaged. The results were shown in Fig. 1. The phantom consists of eight resolution target pattern layers, where each layer was separated by 75  $\mu\text{m}$  in depth, as consistent with Fig. 1(a) showing the B-scan intensity image of the phantom. An *en face* OCT intensity image taken 300  $\mu\text{m}$  above the focus is shown in Fig. 1(b), and the corresponding PR image is shown in Fig. 1(c). As a comparison, those taken near (20  $\mu\text{m}$  below) the focus are shown in Figs. 1(f) and 1(g), respectively. Compared with those acquired near the focus, the intensity and PR images 300  $\mu\text{m}$  above the focus were severely degraded. After CAO implementation, the contrast of the intensity and PR images was significantly improved [Figs. 1(d) and 1(e)] with an OCT intensity image sharpness improvement of 110% and a PR sharpness improvement of 50%, consistent with the intensity and PR profiles shown in Figs. 1(b)–1(i). The wavefront and the relevant Zernike weights implemented on both channels (1 and 2) of the PS-OCT system are shown in Fig. 1(j), demonstrating great similarity between the two, as confirmed by a cross-correlation coefficient of 0.93. This is likely caused by the non-birefringent nature of the phantom and the low NA of the scan objective used. Further investigations on the Zernike weights showed both the defocus (i.e., term Z4) and other low-order aberrations were corrected using CAO. We noticed contrast improvement for those *en face* images taken near to the focus, but with a wavefront characterized by a much-reduced Zernike weight. Specifically, the defocus aberration weight of those images 300  $\mu\text{m}$  above the focus is 30 times higher than images near the focus, revealing the increasing defocus aberration with the increasing distance away from the focus. Overall, the PS-OCT measurements on the OCT phantom (Fig. 1) demonstrate the capability of CAO to correct both the defocus aberration and other low-order aberrations and improve the imaging contrast for PS-OCT measurements.

To further explore how CAO improves PS-OCT imaging contrast for broader applications, we acquired PS-OCT image data from a variety of typically dense and birefringent samples including molded plastics, chicken breast, and human breast tissue. The results of CAO implementation in birefringent molded

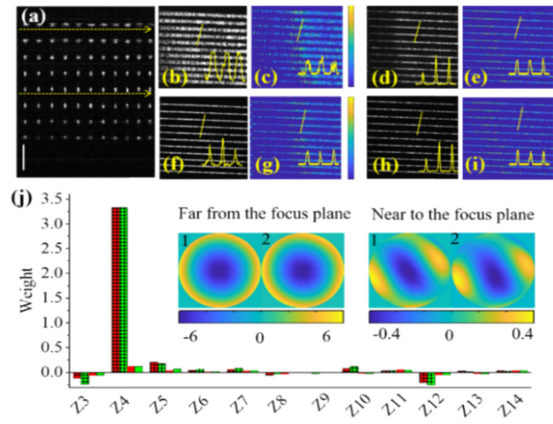


**Fig. 1.** Imaging of an OCT phantom. (a) Cross-sectional OCT intensity image. (b), (d), (f), (h) *En face* intensity and (c), (e), (g), (i) PR images taken 300  $\mu\text{m}$  above and 20  $\mu\text{m}$  below the focus were shown in (b), (c), (f), (g) and (d), (e), (h), (i), and those before and after CAO implementation were in (b)–(e) and (f)–(i), respectively. (j) Wavefront and Zernike weights used on the two channels (Ch1 and Ch2) of PS-OCT measurements to obtain the images of (f), (g) and (h), (i): the Zernike weights implemented on the plane far from (300  $\mu\text{m}$  above) and near (20  $\mu\text{m}$  below) the focus plane are shown in solid diamond and uniform patterns, and those for the two channels of PS-OCT system were shown in red and green, respectively. Scale bar in (a) represents 100  $\mu\text{m}$ .

plastics are shown in Fig. 2. The depth-resolved intensity distribution of the plastic samples is shown in Fig. 2(a). Unlike the 3D OCT phantom characterized by very sparse and visually recognizable patterns, the intensity features of the plastics are vague. The PR [Fig. 2(b)] image, on the other hand, reveals different but complementary features to those in the intensity image, providing additional imaging contrast, and demonstrating the potential of PS-OCT. Looking at the *en face* PS-OCT measurements taken 150  $\mu\text{m}$  below the focus, we found both the intensity [Fig. 2(c)] and PR [Fig. 2(d)] imaging contrast is suboptimal, as evidenced by the blurry features [yellow rectangle indicated regions of Figs. 2(c) and 2(d)], motivating the implementation of CAO for improved imaging of fine features in the plastic samples. The PS-OCT measurements after CAO correction are shown in Figs. 2(e) and 2(f), generating images with sharper imaging contrast [yellow rectangle indicated regions of Figs. 2(e) and 2(f)]. Quantitatively, the sharpness of the OCT intensity [Figs. 2(e)] and PR [Fig. 2(f)] images was improved 36.8% and 13.4%, respectively. The implemented wavefront on both channels of the PS-OCT system [Fig. 2(k), left] and the corresponding Zernike weights [Fig. 2(k)] reveal the various coexisting but CAO-corrected aberrations in the PS-OCT measurements from the molded plastic. In contrast, the CAO implementation effects for those measurements taken near (20  $\mu\text{m}$  above) the focus [Figs. 2(g)–2(j)] were minimal, as evidenced by moderate intensity and PR sharpness improvements of 2.3% and 0.7%, respectively. One notes that the confocal parameter of the objective was calculated to be 100  $\mu\text{m}$ , and CAO improvement is best manifested for planes that are far from ( $> 100 \mu\text{m}$ ) the focal plane [17]. Therefore, for the results below (Figs. 3 and 4), we focus on the CAO effects on those planes far away from ( $> 100 \mu\text{m}$ ) the focus. Using molded plastic as the sample, we compared PR values after using CAO to correct defocus and low-order aberration to those with the

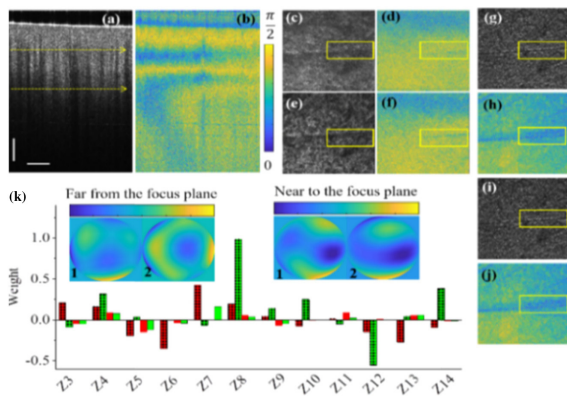


**Fig. 2.** Imaging of molded plastic. (a) Cross-sectional intensity and (b) PR image. (c), (e) *En face* intensity and (d), (f) PR (c), (d) before and (e), (f) after CAO implementation for measurements taken far from ( $150\text{ }\mu\text{m}$  below and indicated by lower, yellow-dotted line) focus. Those taken near the ( $20\text{ }\mu\text{m}$  above and indicated by the upper, yellow-dotted line) focus were shown in (g)–(j) where (g), (h) and (i), (j) were for results before and after CAO implementation. Yellow rectangles in (c)–(j) indicated regions where CAO improvement effects were highlighted. (k) Wavefront and Zernike weights used on the two channels of PS-OCT measurements to obtain the images of (c), (f) and (i)–(j): the Zernike weights implemented on the plane far from and near the focus plane are shown in solid diamond and uniform patterns, and those for the two channels of PS-OCT system were shown in red and green. Scale bars in (a) represent  $150\text{ }\mu\text{m}$ . Color bar ranges from  $-3$  to  $3$  and  $-1$  to  $1$  for the wavefront implemented on planes far from and near the focus, respectively.

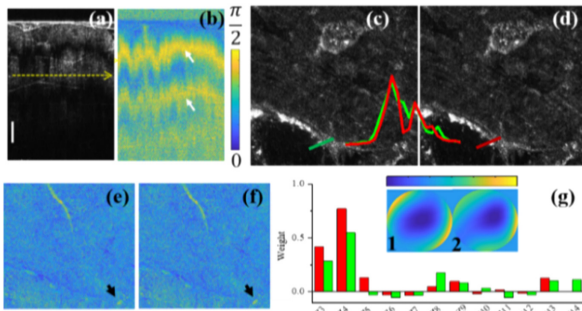


**Fig. 3.** Imaging of *ex vivo* chicken breast tissue. (a) Cross-sectional intensity and (b) PR images, showing strong PR as highlighted by the white arrows in (b). (c), (d) *En face* intensity and (e), (f) PR images taken  $150\text{ }\mu\text{m}$  below the focus, (c), (e) before and (d), (f) after CAO implementation. The intensity profiles corresponding to those before and after CAO implementation were shown in green and red colors. The black arrows in (e), (f) indicate the area where CAO improves PR sharpness. (g) Wavefront and Zernike weights used on the two channels of PS-OCT measurements to obtain (d), (f). Scale bar represents  $200\text{ }\mu\text{m}$ . Color bar [within sub-figure (g)] ranges from  $-1$  to  $2.5$ .

focus shifted to the plane of interest ( $130\text{ }\mu\text{m}$  below the focus), experimentally. The PR maps show a correlation coefficient of  $0.91$ , demonstrating the closeness of the two PR maps measured. Overall, the results in Fig. 2 initially demonstrate the adaptability of CAO for improving PS-OCT imaging contrast from a dense birefringent sample.

Figure 3 shows PS-OCT measurements from *ex vivo* chicken breast tissue. The standard intensity image [Fig. 3(a)] reveals

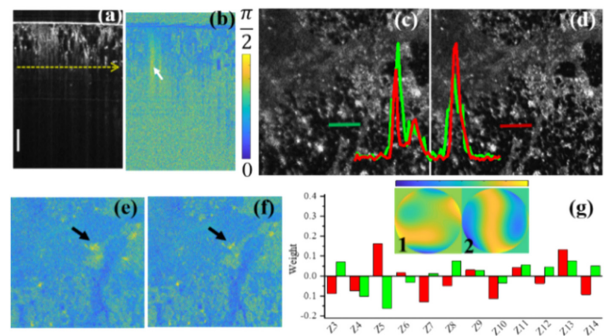


**Fig. 4.** Imaging of *ex vivo* human breast tumor tissue. (a) Cross-sectional intensity and (b) PR images. White arrow highlighted region in (b) shows strong PR that could be attributed to the remaining normal stroma that has not been replaced by tumor invasion and remodeling. (c), (d) *En face* intensity and (e), (f) PR images taken  $150\text{ }\mu\text{m}$  below the focus, (c), (e) before and (d), (f) after CAO implementation. The intensity profiles corresponding to those before and after CAO implementation were shown in green and red colors, respectively. The black arrows in (e), (f) indicate the area where CAO improves PR sharpness. (g) Wavefront and Zernike weights used on the two channels of PS-OCT measurements to obtain the images of (d), (f). Scale bar represents  $200\text{ }\mu\text{m}$ . Colorbar in (g) ranges from  $-1.75$  to  $0.75$ .

different brightness along the tissue depth, indicating refractive index and scattering variations of the chicken breast tissue. The PS-OCT PR [Fig. 3(b)] shows strong birefringence (regions highlighted by white arrows) arising from the form birefringence of the muscle fiber within the chicken breast tissue. We then compared the *en face* PS-OCT measurements with [Figs. 3(d) and 3(f)] and without [Figs. 3(c) and 3(e)] CAO correction. CAO indeed generates better PS-OCT imaging contrast. For instance, CAO enables visualization of finer structures (profiles along the yellow-dotted lines: the red and green profiles correspond to those with and without CAO correction) from the standard OCT intensity and PR (black arrow indicated areas). Further sharpness calculation shows an improvement of  $26.2\%$  and  $2.8\%$ , respectively, for the standard OCT intensity [Fig. 3(c)] and PR [Fig. 3(e)], reaffirming the aberration correction capability of CAO on real biological samples with strong birefringence.

We also explored the capability of CAO correction on PS-OCT measurements of clinically relevant samples: *ex vivo* tumor (invasive ductal carcinoma) tissue from the human breast (Fig. 4). Figures 4(a) and 4(b) show the B-scan intensity and PR images, demonstrating moderate scattering and low PR, consistent with our previous findings [13]. In the PR image, we noticed a small portion of the image (white arrow highlighted region) shows strong PR, which could be attributed to the remaining normal stroma that has not been replaced by tumor invasion and remodeling. Further *en face* viewing of the PR [Fig. 4(e)] shows an overall low PR with small regions (black arrow highlighted region) characterized by relatively strong PR. This finding is consistent with that of the depth-resolved B-scan PR image. CAO implementation shows a sharpness improvement of  $18.2\%$  and  $6.8\%$  for the standard OCT intensity [Fig. 4(c)] and PR [Fig. 4(e)], respectively, confirming the suitability of CAO for improving the imaging contrast of clinically relevant samples. The profile visualization [Figs. 4(c) and 4(d)] co-validates the enhanced imaging contrast enabled by

**Table 1.** PS-OCT Measurements of Sharpness Changes with CAO Correction<sup>a</sup>

	Intensity (%)	PR (%)	Optical Axis (%)
Molded plastics piece ( <i>n</i> = 5)	+ (30.5 ± 11.2)	+ (10.8 ± 4.2)	+ (7.8 ± 2.2)
Chicken breast tissue ( <i>n</i> = 4)	+ (23.4 ± 5.9)	+ (3.6 ± 1.4)	+ (1.9 ± 1.6)
Human breast tumor tissue ( <i>n</i> = 6)	+ (15.9 ± 6.2)	+ (5.7 ± 2.4)	+ (4.2 ± 1.6)

<sup>a</sup>The mean and standard deviations of the sharpness changes were summarized.

CAO. One notes that the red profile after CAO shows a reduced intensity for the left peak but an increased intensity for the right peak, which is likely caused by the global optimization of the image sharpness over the whole field-of-view. Further local CAO implementation over sub-regions of the field-of-view warrants further investigation to increase the image SNR further [15]. Overall, this improved image quality could potentially benefit the detection of residual cancer in breast tumor margins, where polarization information can aid in the differentiation between normal and diseased tissue by identifying birefringent regions as collagenous stroma.

To further evaluate how CAO improves PS-OCT measurement sharpness, we acquired additional PS-OCT measurements from five different sites of a molded plastics piece, five different chicken breast tissues, and five additional human breast tumor tissues. The mean and standard deviations of the sharpness changes of intensity, PR, and optical axis are summarized in Table 1, confirming the effectiveness of CAO for improving PS-OCT measurement sharpness. One notes that the sharpness improvement for the birefringence [18] and degree of polarization uniformity (DOPU) was minor. This is probably caused by the oversimplified assumption of the sample as a pure retarder when converting the measured Jones vector to the Jones matrix and deriving the birefringence thereof [19]. A more robust derivation of the Jones matrix using a Jones matrix PS-OCT system [20] may help justify the performance of CAO on improving the sharpness of the birefringence measurement. The minor improvement of CAO on DOPU is due to the spatial kernel inherently needed, counteracting the CAO improvement effects.

In summary, for the first time, to the best of our knowledge, we have demonstrated CAO correction of PS-OCT measurements from birefringent samples and biological tissues (chicken and human). The improved PS-OCT imaging contrast by CAO not only improves the capability of PS-OCT for tissue differentiation but also reveals more fine features within the tissue microenvironment. We believe the emergence of high-speed megahertz swept sources [21] and swept source driven PS-OCT systems [20], as well as the use of fast, parallel algorithms utilizing graphics processing units, will allow future real-time CAO implementation on the volumetric PS-OCT measurements.

**Funding.** National Cancer Institute (R01 CA213149); National Institute of Biomedical Imaging and Bioengineering (R01 EB023232).

**Acknowledgment.** J. Wang was supported by The Carle Foundation Hospital-Beckman Institute Postdoctoral Fellows Program. We thank Darold Spillman for technical support, Drs. Anna Higham and Kimberly Cradock for providing human surgical tissue specimens as part of their standard practice, and the human subjects for volunteering to contribute tissue specimens for this research. We also thank the study coordinators and Research Office at Carle Foundation Hospital. Additional information can be found at <http://biophotonics.illinois.edu>.

**Disclosures.** S.A.B. is co-founder of Diagnostic Photonics, Inc., which is commercializing ISAM and OCT for intraoperative imaging applications.

**Data Availability.** Data underlying the results presented in this paper are not publicly available at this time but may be obtained from the authors upon reasonable request and through a collaborative research agreement.

## REFERENCES

- D. Huang, E. A. Swanson, C. P. Lin, J. S. Schuman, W. G. Stinson, W. Chang, M. R. Hee, T. Flotte, K. Gregory, C. A. Puliafito, and J. G. Fujimoto, *Science* **254**, 1178 (1991).
- W. Drexler, U. Morgner, R. K. Ghanta, F. X. Kärtner, J. S. Schuman, and J. G. Fujimoto, *Nat. Med.* **7**, 502 (2001).
- J. Wang, Y. Xu, and S. A. Boppart, *J. Biomed. Opt.* **22**, 121711 (2017).
- T. H. Tsai, C. L. Leggett, A. J. Trindade, A. Sethi, A. F. Swager, V. Joshi, B. H. Mashimo, N. S. Nishioka, and E. Namati, *J. Biomed. Opt.* **22**, 121716 (2017).
- T. S. Ralston, D. L. Marks, P. S. Carney, and S. A. Boppart, *Nat. Phys.* **3**, 129 (2007).
- S. G. Adie, B. W. Graf, A. Ahmad, P. S. Carney, and S. A. Boppart, *Proc. Natl. Acad. Sci. USA* **109**, 7175 (2012).
- P. Paritosh, Y.-Z. Liu, F. A. South, and S. A. Boppart, *Opt. Lett.* **41**, 3324 (2016).
- F. A. South, E. J. Chaney, M. Marjanovic, S. G. Adie, and S. A. Boppart, *Biomed. Opt. Express* **5**, 3417 (2014).
- J. Strasswimmer, M. C. Pierce, H. Park, V. Neel, and J. F. De Boer, *J. Biomed. Opt.* **9**, 292 (2004).
- J. J. Pasquesi, S. C. Schlachter, M. D. Boppart, E. J. Chaney, S. J. Kaufman, and S. A. Boppart, *Opt. Express* **14**, 1547 (2006).
- M. R. Strąkowski, J. Pluciński, M. Jędrzejewska-Szczerska, R. Hypszer, M. Maciejewski, and B. B. Kosmowski, *Sens. Actuators A, Phys.* **142**, 104 (2008).
- J. F. De Boer, C. K. Hitzenberger, and Y. Yasuno, *Biomed. Opt. Express* **8**, 1838 (2017).
- F. A. South, Y. Z. Liu, Y. Xu, N. D. Shemonski, P. S. Carney, and S. A. Boppart, *Appl. Phys. Lett.* **107**, 211106 (2015).
- J. Wang, Y. Xu, K. J. Mesa, A. South, E. J. Chaney, D. R. Spillman, R. Barkalifa, M. Marjanovic, P. S. Carney, A. M. Higham, Z. G. Liu, and S. A. Boppart, *Biomed. Opt. Express* **9**, 6519 (2018).
- F. A. South, Y. Z. Liu, P. C. Huang, T. Kohlfarber, and S. A. Boppart, *Opt. Lett.* **44**, 1186 (2019).
- J. A. Kubby, *Adaptive Optics for Biological Imaging* (CRC Press, 2013), pp. 200–202.
- J. A. Izatt and M. A. Choma, *Optical Coherence Tomography* (Springer, 2008), p. 47.
- M. Villiger, D. Lorenser, R. A. McLaughlin, B. C. Quirk, R. W. Kirk, B. E. Bouma, and D. D. Sampson, *Sci. Rep.* **6**, 28771 (2016).
- C. Fan and G. Yao, *Opt. Lett.* **37**, 1415 (2012).
- M. J. Ju, Y. J. Hong, S. Makita, Y. Lim, K. Kurokawa, L. Duan, M. Miura, S. Tang, and Y. Yasuno, *Opt. Express* **21**, 19412 (2013).
- Z. Zhi, W. Qin, J. Wang, W. Wei, and R. K. Wang, *Opt. Lett.* **40**, 1779 (2015).